

## Modelling a growth instability in a stressed solid

A-V Phan<sup>1</sup>, T Kaplan<sup>1</sup>, L J Gray<sup>1</sup>, D Adalsteinsson<sup>2</sup>, J A Sethian<sup>3</sup>,  
W Barvosa-Carter<sup>4</sup> and M J Aziz<sup>5</sup>

<sup>1</sup> Computer Science and Mathematics Division, Oak Ridge National Laboratory, Oak Ridge, TN 37831-6367, USA

<sup>2</sup> Department of Mathematics, University of North Carolina, Chapel Hill, NC 27599, USA

<sup>3</sup> Department of Mathematics, University of California, Berkeley, CA 94720, USA

<sup>4</sup> HRL Laboratories, 3011 Malibu Canyon Road, Malibu, CA 90265, USA

<sup>5</sup> Division of Engineering and Applied Sciences, Harvard University, Cambridge, MA 02138, USA

Received 17 January 2001, accepted for publication 26 April 2001

### Abstract

The growth of crystalline silicon from the amorphous phase in the presence of an applied stress is modelled using advanced numerical methods. The crystal region is modelled as a linear elastic solid and the amorphous as a viscous fluid with a time-dependent viscosity to reflect structural relaxation. Appropriate coupling conditions across the boundary are defined, and both problems are solved using a symmetric-Galerkin boundary integral method. The interface is advanced in time using the level set technique. The results match well with experiments and support the proposed kinetic mechanism for the observed interface growth instability.

### 1. Introduction

It is well known that the surface of a non-hydrostatically stressed solid is subject to an elastic strain energy-driven morphological instability [1–3]. However, up until recently, little attention had been paid to the effect that stress has on the *mobilities* of the interface atoms involved in the growth process, and the resulting effect on the interface morphology. In two recent papers studying the amorphous/crystal silicon system [4, 5], both experiments and simulations were used to demonstrate that the kinetic effect, i.e. the effect of stress on the mobilities, is responsible for the observed growth instability. Furthermore, these results were shown to be consistent with a linear stability analysis by Voorhees and Aziz [6].

Although the initial simulations in [4, 5] were sufficient to establish the dominance of the kinetic effect, they were far from a complete analysis. In particular, these calculations simply assumed all stress was relaxed in the amorphous solid, i.e. that the interface was a traction-free surface. In this paper, we significantly improve both the model and numerical methods to provide much more detailed simulations of the growth process. Specifically, the stress in the amorphous solid is modelled as both a viscous fluid (Stokes flow) and an elastic solid, and improvements have been made in the modelling of the phase transformation at the crystal/amorphous interface. These include a more accurate model of the angular dependence

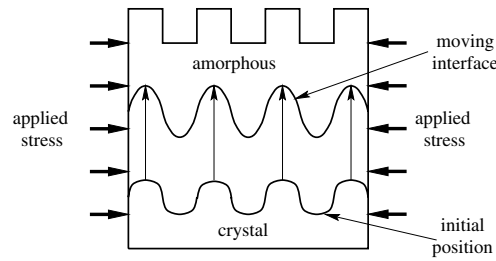


**Figure 1.** Crystal growth in a furnace.

of the growth velocity as well as newer values for some of the physical parameters. The numerical accuracy has also been significantly improved by replacing a marker particle method for tracking the moving boundary with the level set method [7]. The elasticity and Stokes solutions are obtained from a boundary integral analysis, and the combination with the level set is very effective.

The present paper is organized as follows. The experiments and mathematical model for the silicon system are described in section 2. The numerical methods are discussed in section 3 and the simulations in section 4. In section 5, the numerical results are compared with experiment and analysed. Concluding remarks are in section 6.

## 2. Experiment and model

A schematic of the experimental set-up is shown in figure 1. A rippled interface was fabricated by ion implantation of a silicon wafer with a lithographically corrugated free surface. Several Si(001) wafers 1 mm thick were patterned using x-ray lithography. The free surfaces of the samples were patterned with lines parallel to [100] and a repeat length of  $\lambda = 400$  nm. Each wafer's surface was then amorphized by ion implantation ( $\text{Si}^+$ , 90 keV,  $2 \times 10^{15} \text{ cm}^{-2}$ , 77 K) to form a continuous layer of amorphous Si. The samples were then annealed at 520 °C while a compressive stress was applied in the plane of the interface producing a uniaxial stress of  $-0.5$  GPa. A control series of samples was annealed under zero stress. Another single sample [5] was annealed while being loaded between two rings of different size to produce tension in the amorphous side of the sample. This configuration resulted in a uniform biaxial stress of  $+0.5$  GPa in the plane of the interface in the region within the smaller ring. All samples were analysed using cross sectional transmission electron microscopy to measure the interface amplitude and final depth.

The rippled interface separating the crystal and amorphous silicon is approximated by a sine wave with a wavelength of 400 nm and a peak-to-peak amplitude of 20 nm. By symmetry, only a half wavelength segment of 200 nm need be treated. The silicon crystal is modelled as an isotropic linear elastic solid. Since silicon is a cubic solid, Voight averaging is used to determine the best fit for the isotropic elastic constants; shear modulus  $G_c = 0.6814 \times 10^{11}$  Pa and Poisson's ratio  $\nu_c = 0.2174$  [8]. The amorphous solid is modelled as a viscous fluid with a time-dependent viscosity as given in figure 6 later [9]. For completeness, we also consider two limiting cases that provide upper and lower bounds for the simulations. Modelling the amorphous solid as an isotropic linearly elastic solid with elastic constants  $G_a = 0.79G_c$  and  $\nu_a = \nu_c$  [10] overestimates the stress in the amorphous phase, while modelling the amorphous solid as stress free (i.e. a free surface on the crystal silicon at the interface) underestimates the stress. The stress-free amorphous assumption was used in the original simulations published in [4, 5].

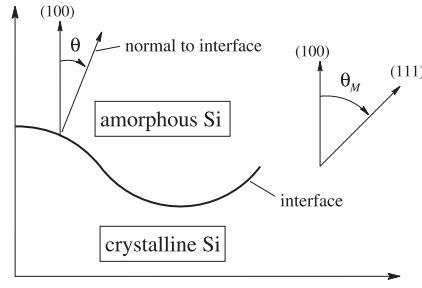


Figure 2. Angles  $\theta$  and  $\theta_M$ .

A transition state theory based model is used to describe the phase transformation at the silicon crystal/amorphous interface. This model assumes that a single, unimolecular, defect mediated mechanism controls the silicon crystal to amorphous transition rate in the temperature range of interest. Within this model [9] the growth velocity normal to the interface at any point on the interface can be expressed as

$$v = v_0(\theta) \exp\left(\frac{\sigma V^* - E^*}{k_B T}\right) \sinh\left(\frac{\Delta G_{ac}}{2k_B T}\right). \quad (1)$$

The prefactor  $v_0(\theta)$  contains factors such as the attempt frequency and defect hopping distance and is a function of interface orientation  $\theta$  (see figure 2). From experiments [11, 12] we determine the angular dependence of the velocity function to be

$$v_0(\theta) = \frac{v_{100}}{2} \left[ (1 - \alpha) \cos\left(\frac{\pi\theta}{\theta_M}\right) + (1 + \alpha) \right] \quad \alpha = \frac{v_{111}}{v_{100}} \quad (2)$$

where  $\theta$  is the angle between the normal at a point on the interface and the (100) axis of crystalline Si, and  $v_{100}$  and  $v_{111}$  are the relative growth velocities for interfaces oriented in the (100) and (111) directions respectively.  $\theta_M$  is the angle between the direction of the (111) axis and that of the (100) axis. From [11],  $\alpha = 0.05v_{100}$ , and  $\theta_M = 54.7^\circ$  and from [13]  $v_{100} = 3.1 \times 10^8 \text{ cm s}^{-1}$ .

The first exponential factor in equation (1) represents the temperature dependence of the interface mobility.  $E^* = 2.68 \text{ eV}$  is the activation energy [13],  $V^*$  is the activation strain,  $\sigma$  is the stress at the interface evaluated from the crystal side,  $T$  is the temperature, and  $k_B$  is the Boltzmann constant. The activation strain term can be written as

$$\begin{aligned} \sigma V^* &= \sigma_{xx} V_{xx} + \sigma_{yy} V_{yy} + 2\sigma_{xy} V_{xy} \\ V_{xx} &= 0.14\Omega \quad V_{yy} = -0.35\Omega \quad V_{xy} = 0 \end{aligned} \quad (3)$$

where  $x$  and  $y$  are aligned along the (100) and (001) directions,  $\Omega = 12.0 \times 10^{-6} \text{ m}^3 \text{ mol}^{-1}$  is the molar volume of crystalline silicon [9, 14, 15], and  $\sigma_{ij}$  are the corresponding elements of the stress tensor. The assumption that the stress state on the amorphous side of the interface does not influence the growth rate has some experimental support [16] but it is by no means a closed question.

The sinh term is the free energy driving force for growth and  $\Delta G_{ac}$  is the difference in free energy between amorphous and crystalline silicon. The free energy is composed of three terms,

$$\Delta G_{ac}(T, \kappa, \sigma) = \Delta G_{ac}^o(T) + \Delta G_{\kappa} + \Delta G_{\sigma}. \quad (4)$$

The first term

$$\Delta G_{ac}^o(T) = (g_T T + g_0) N_0 \quad (5)$$

is the temperature-dependent free energy change per unit volume from amorphous to crystalline silicon [17].  $g_T = -0.274 \times 10^{-4}$  eV/(atom K),  $g_0 = 0.1$  eV/atom,  $N_0$  is Avogadro's number  $= 6.025 \times 10^{23}$  atoms/mol, and  $T$  is the temperature in degrees Kelvin. The change in free energy due to interface curvature is

$$\Delta G_\kappa = \gamma \kappa \Omega \quad (6)$$

where  $\gamma = 0.49$  eV m<sup>-2</sup> is the interfacial energy [18, 19], and  $\kappa$  is the curvature, reckoned positive for a convex crystal.

Lastly, the free energy change due to stress can be separated into two contributions

$$\Delta G_\sigma = \Delta G_\sigma^{(1)} + \Delta G_\sigma^{(2)}. \quad (7)$$

The first contribution,  $\Delta G_\sigma^{(1)}$ , is due to changes in the total energy of the crystal when a volume of materials is crystallized. Upon crystallization, the volume of the system (crystal + amorphous) changes by  $\Delta V_c$ . If the system is held under stress by a set of external forces, then the free energy of crystallization will change because the system must do work against these forces. From [20],

$$\Delta V_c = 0.117 \Omega \quad (8)$$

and the change in free energy per volume of crystal is

$$\Delta G_\sigma^{(1)} = p \Delta V_c = \frac{-\text{Tr}(\sigma) \Delta V_c}{3} = -(\sigma_{xx} + \sigma_{yy}) 0.117 \frac{\Omega}{3} \quad (9)$$

where we have assumed plane stress.

The second term,  $\Delta G_\sigma^{(2)}$ , arises from the change in the internal strain energy of the system when a volume of material crystallizes. The change in internal energy per unit volume crystallized is

$$\Delta G_\sigma^{(2)} = \sigma_{ij}^a \epsilon_{ij}^a \frac{\Omega}{2} - \sigma_{ij}^c \epsilon_{ij}^c \frac{\Omega}{2} = (\epsilon_{ij}^a C_{ijkl}^a \epsilon_{kl}^a - \epsilon_{ij}^c C_{ijkl}^c \epsilon_{kl}^c) \frac{\Omega}{2} \quad (10)$$

where  $C_{ijkl}^a$  and  $C_{ijkl}^c$  are the elastic constants. Crystalline silicon is cubic and the non-zero elastic constants are given below in standard cubic notation [21]:

$$C_{11}^c = 1.658 \times 10^{12} \text{ Pa} \quad C_{12}^c = 0.639 \times 10^{12} \text{ Pa} \quad C_{44}^c = 1.592 \times 10^{12} \text{ Pa}. \quad (11)$$

Amorphous silicon is isotropic with shear modulus  $G = 0.5383 \times 10^{12}$  Pa, and Poisson's ratio  $\nu = 0.2174$  [10]. For inclusion in equation (10), they are converted to cubic form [22] below

$$C_{11}^a = 1.491 \times 10^{12} \text{ Pa} \quad C_{12}^a = 0.414 \times 10^{12} \text{ Pa} \quad C_{44}^a = 1.077 \times 10^{12} \text{ Pa}. \quad (12)$$

Note that the solid-state physics and engineering literatures employ different definitions for the off-diagonal strains  $\epsilon_{ij}$ . The convention in solid-state physics [23] is  $\epsilon_{ij} = u_{i,j} + u_{j,i}$  without the 1/2 factor employed elsewhere ( $u_i$  are the components of the displacement vector, the subscript after the comma indicating differentiation in that direction). Thus  $C_{44}$  in engineering notation is twice as big as  $C_{44}$  in solid-state physics notation. We employ engineering notation in this paper. In the simulations presented, the contribution from the amorphous silicon to  $\Delta G_\sigma^{(2)}$  is not included because a surface stress evaluator for the viscous amorphous code has not been constructed as yet. For consistency, we do not include it in the elastic model of the amorphous phase as well. Since, the  $\Delta G_\sigma^{(2)}$  term is relatively small, the neglected amorphous contribution should have a negligible effect on the simulations.

### 3. Numerical methods

#### 3.1. Symmetric-Galerkin boundary integral analysis

In the simulations reported below, a boundary integral formulation is employed to solve the elasticity and Stokes flow problems. The symmetric-Galerkin approximation is used to reduce these continuous equations to a finite system. This section presents a quick overview of this symmetric-Galerkin boundary integral method (SGBIM). A good introduction to this technique is provided in the recent text by Bonnet [24], and a recent review by Bonnet *et al* [25] provides an excellent summary and references to the literature.

*3.1.1. SGBIM for linear elasticity.* The boundary integral equation (BIE) for linear elasticity, without body forces, is given by Rizzo [26]. For a source point  $P$  exterior to the domain, this equation takes the form

$$U(P) \equiv \int_{\Gamma} U_{kj}(P, Q)\tau_j(Q) dQ - \int_{\Gamma} T_{kj}(P, Q)u_j(Q) dQ = 0 \quad (13)$$

where  $Q$  is the field point,  $\tau_j$  and  $u_j$  are traction and displacement vectors, and the kernel tensors  $U_{kj}$  and  $T_{kj}$  are the appropriate (Kelvin) fundamental solutions.

For plane strain problems (see [26] for example),

$$U_{kj} = \frac{1}{8\pi G(1-\nu)} [r_{,k}r_{,j} - (3-4\nu)\delta_{kj} \ln(r)] \quad (14)$$

$$T_{kj} = -\frac{1}{4\pi(1-\nu)r} \left[ \{(1-2\nu)\delta_{kj} + 2r_{,k}r_{,j}\} \frac{\partial r}{\partial n} - (1-2\nu)(n_j r_{,k} - n_k r_{,j}) \right] \quad (15)$$

where  $\nu$  is Poisson's ratio,  $G$  is the shear modulus,  $\delta_{ij}$  is the Kronecker delta,  $r_k = x_k(Q) - x_k(P)$ ,  $r^2 = r_i r_i$ ,  $r_{,k} = r_k/r$  and  $\partial r/\partial n = r_{,i} n_i$ .

It can be shown that the limit of the right-hand side of equation (13) as  $P$  approaches the boundary exists. The result is the boundary displacement at  $P$ , and thus equation (13) is called the BIE for displacement. From now on, for  $P \in \Gamma$ , the BIE is understood in this limiting sense.

As  $P$  is off the boundary, the kernel functions are not singular and it is permissible to differentiate equation (13) with respect to  $P$ , yielding the hypersingular BIE (HBIE) for the displacement gradient

$$\int_{\Gamma} U_{kj,L}(P, Q)\tau_j(Q) dQ - \int_{\Gamma} T_{kj,L}(P, Q)u_j(Q) dQ = 0. \quad (16)$$

As usual, the HBIE for boundary stress is of interest. This equation follows from the strain-displacement equation and Hooke's law, and taking the appropriate linear combinations of equation (16) results in

$$S(P) \equiv \int_{\Gamma} D_{kjil}(P, Q)\tau_j(Q) dQ - \int_{\Gamma} S_{kjil}(P, Q)u_j(Q) dQ = 0. \quad (17)$$

The new kernel tensors are

$$D_{kj\ell} = \frac{1}{4\pi(1-\nu)r} [(1-2\nu)(\delta_{kj}r_{,\ell} + \delta_{j\ell}r_{,k} - \delta_{\ell k}r_{,j}) + 2r_{,k}r_{,j}r_{,\ell}] \quad (18)$$

$$S_{kj\ell} = \frac{G}{2\pi(1-\nu)r^2} \left[ 2 \frac{\partial r}{\partial n} \{ (1-2\nu)\delta_{\ell k}r_{,j} + \nu(\delta_{kj}r_{,\ell} + \delta_{j\ell}r_{,k}) - 4r_{,k}r_{,j}r_{,\ell} \} \right. \\ \left. + 2\nu(n_k r_{,j}r_{,\ell} + n_{\ell} r_{,k}r_{,j}) + (1-2\nu)(2n_j r_{,\ell}r_{,k} + \delta_{kj}n_{\ell} + \delta_{j\ell}n_k) \right. \\ \left. - (1-4\nu)\delta_{\ell k}n_j \right]. \quad (19)$$

In the Galerkin approximation, equations (13) and (17) are multiplied by a weighting function and integrated over the boundary a second time,

$$\int_{\Gamma} \Psi_m(P) \mathcal{U}(P) = 0 \quad (20)$$

$$\int_{\Gamma} \Psi_m(P) \mathcal{S}(P) = 0. \quad (21)$$

The weighting functions  $\Psi_m$  are the shape functions employed to interpolate the boundary tractions and displacements from the nodal values. In this work, a quadratic interpolation is used. The prescription to obtain a symmetric coefficient matrix, and hence the name symmetric-Galerkin, is to employ equation (20) on the part of the boundary with prescribed displacements, and equation (21) on the boundary segment with prescribed tractions. The symmetry is a consequence of the symmetry properties of the four kernel functions.

Galerkin enforces the integral equations ‘on average’, rather than the pointwise approach of the traditional collocation approximation. Apart from symmetry, a key advantage of this technique is that the second boundary integration counterbalances the differentiation that created the hypersingular kernel. Galerkin therefore only involves singular integrals which are effectively Cauchy type at worst. Thus, unlike collocation, there is no interpolation smoothness constraint required for the existence of the hypersingular  $S_{kjl}$  integral [27–33], and standard  $C^0$  elements can be employed.

The primary disadvantage of the Galerkin procedure is the additional computational work required by the second boundary integration. However, this can be somewhat mitigated by exploiting symmetry, both in the matrix construction [34] and solution phases [35]. A second perceived disadvantage is the complexity of the singular integral evaluation. A number of techniques are available [36–38]; in this work we employ a ‘direct’ evaluation method which combines both analytical and numerical quadrature [39].

*3.1.2. SGBIM for Stokes flow.* For a source point  $P$  located inside a selected area of flow, the boundary integral and hypersingular boundary integral equations are written as [40]

$$v_k(P) = \int_{\Gamma} \bar{U}_{kj}(P, Q) \tau_j(Q) dQ - \int_{\Gamma} \bar{T}_{kj}(P, Q) v_j(Q) dQ \quad (22)$$

$$\sigma_{k\ell}(P) = \int_{\Gamma} \bar{D}_{kj\ell}(P, Q) \tau_j(Q) dQ - \int_{\Gamma} \bar{S}_{kj\ell}(P, Q) v_j(Q) dQ \quad (23)$$

where  $\tau_j$ ,  $v_j$ , and  $\sigma_{k\ell}$  are traction, flow velocity, and stress tensor respectively, and  $\bar{U}_{kj}$ ,  $\bar{T}_{kj}$ ,  $\bar{D}_{kj\ell}$ , and  $\bar{S}_{kj\ell}$  are the kernel tensors for Stokes flow,

$$\bar{U}_{kj} = \frac{1}{4\pi\mu} [r_{,k}r_{,j} - \delta_{kj} \ln(r)] \quad (24)$$

$$\bar{T}_{kj} = -\frac{1}{\pi r} r_{,k}r_{,j} \frac{\partial r}{\partial n} \quad (25)$$

$$\bar{D}_{kj\ell} = \frac{1}{\pi r} r_{,k}r_{,j}r_{,\ell} \quad (26)$$

$$\bar{S}_{kj\ell} = -\frac{\mu}{\pi r^2} \left[ (8r_{,k}r_{,j}r_{,\ell} - \delta_{j\ell}r_{,k} - \delta_{kj}r_{,\ell}) \frac{\partial r}{\partial n} - (r_{,k}n_{\ell} + r_{,\ell}n_k)r_{,j} - \delta_{k\ell}n_j \right] \quad (27)$$

where  $\mu$  is the viscosity.

Observe that these kernels can be obtained by substituting  $G$  and  $\nu$  in the kernels for elasticity ((14), (15), (18), and (19)) with  $\mu$  and 0.5, respectively. Thus, the SGBIM code for elasticity can be employed to solve Stokes flow problems by using viscosity  $\mu$  as shear modulus  $G$  and  $\nu = 0.5$ .

3.1.3. *Surface stress evaluation.* In order to compute the velocity of the amorphous/crystalline interface, solution of the specified boundary value problems does not suffice. From equation (3) the velocity is a function of the complete stress tensor on the crystal side of the interface, whereas the boundary integral solution only supplies the normal component (traction). The tangential components can be expressed by using the interior limit form of equation (17),

$$\sigma_{kl}(P) = \int_{\Gamma} D_{kjl}(P, Q)\tau_j(Q) dQ - \int_{\Gamma} S_{kjl}(P, Q)u_j(Q) dQ \quad (28)$$

and the boundary integral solution provides the complete boundary traction  $\tau_j(Q)$  and displacement vectors  $u_j(Q)$ . However, direct evaluation of  $\sigma_{kl}(P)$  from this hypersingular equation is nevertheless problematic, due to, as noted above, the smoothness constraint on  $u_j(Q)$ . In this work the stress tensor is obtained by once again employing a Galerkin procedure to reduce the order of the singularities [41]. This method results in a system of linear equations for the tensor everywhere on the boundary. A feature of this approach exploited herein is that the system of equations naturally terminates at boundary corners. Thus, the interface stress tensor can be evaluated without computing this quantity elsewhere on the boundary.

### 3.2. Level set methods

A traditional technique for tracking moving interfaces is known as the marker particle method for which the interface propagation during an incremental time step  $\Delta t$  is monitored by shifting each interfacial marker  $\mathbf{x}$  in its normal direction  $\mathbf{n}$  by an amount  $v(\mathbf{x})\Delta t$ . This method can be highly accurate for small-scale motions of the interfaces because of their adaptive nature. However, under complex motions of the interface, the technique can suffer from instability and topological limitations because it follows a local representation of the front, rather than a global one that takes into account the proper entropy conditions and weak solutions.

Level set methods are computational techniques, introduced by Osher and Sethian [42], for tracking moving interfaces in two and three dimensions. These techniques work by embedding the propagating interface as the zero level set of a time-dependent, implicit function, and then solving the resulting equations of motion in a fixed grid Eulerian setting. They have been used with considerable success in a wide collection of settings, including fluid mechanics, crystal growth, combustion, and medical imaging. A general overview of the theory, numerical approximation, and range of applications may be found in [7].

Level set methods rely in part on the theory of curve and surface evolution given in [43] and on the link between front propagation and hyperbolic conservation laws discussed in [44]. They recast interface motion as a time-dependent Eulerian initial value partial differential equation, and rely on viscosity solutions to the appropriate differential equations to update the position of the front, using an interface velocity that is derived from the relevant physics both on and off the interface. These viscosity solutions are obtained by exploiting schemes from the numerical solution of hyperbolic conservation laws. Level set methods are specifically designed for problems involving topological change, dependence on curvature, formation of singularities, and a host of other issues that often appear in interface propagation techniques. Over the past few years, various aspects of these techniques have been refined to the point where a general computational approach to arbitrary front propagation problems can be developed. This general computational approach allows one to track the motion of very complex interfaces, with significant and delicate coupling between the relevant physics and the interface motion.

Level set methods rely on two central embeddings. First, the embedding of the interface as the zero level set of a higher-dimensional function, and second, the embedding (or extension) of the interface's velocity to this higher-dimensional level set function. More precisely, given a

moving closed hypersurface  $\Gamma(t)$ , that is,  $\Gamma(t = 0) : [0, \infty) \rightarrow R^N$ , propagating with a speed  $v$  in its normal direction  $\mathbf{n}$ , it is desired to produce an Eulerian formulation for the motion of the hypersurface propagating along its normal direction with speed  $v$ , where  $v$  can be a function of various arguments, including the curvature, normal direction, etc. Let  $\pm d$  be the signed distance to the interface. If this propagating interface is embedded as the zero level set of a higher-dimensional function  $\phi$ , that is, let  $\phi(\mathbf{x}, t = 0)$ , where  $\mathbf{x} \in R^N$ , be defined by

$$\phi(\mathbf{x}, t = 0) = \pm d \quad (29)$$

then an initial value partial differential equation can be obtained for the evolution of  $\phi$ , namely

$$\phi_t + v^{\text{ext}} |\nabla \phi| = 0 \quad (30)$$

$$\phi(\mathbf{x}, t = 0) \text{ given.} \quad (31)$$

This is known as the level set equation, given in [42]. Since we are interested in the interface evolution, in equation (30),  $v^{\text{ext}}$  is some velocity field defined for all the level sets, not just the zero level set corresponding to the interface itself. In other words,

$$v^{\text{ext}} = v \quad \text{on } \phi = 0.$$

This new velocity field  $v^{\text{ext}}$  is known as the ‘extension velocity’. The correct extension velocity is one that satisfies the equation

$$\nabla v^{\text{ext}} \cdot \nabla \phi = 0. \quad (32)$$

The solution  $v^{\text{ext}}$  to equation (32) can be produced using a variant on the fast marching method [46] that does not require the computation of field values away from the interface.

The above equations are all discretized on a fixed, Eulerian mesh, and then approximated using conservative schemes designed to accurately approximate the correct extension velocity solution of the equations of motion. Geometric quantities, such as the local curvature, normal direction, boundary integrals, etc, may all be accurately approximated in this fixed setting using either finite-element or finite-difference formulations. Therefore, the level set methods not only accurately characterize and advance the moving interfaces, but also provide accurate local curvatures and normals which are required by the computation of the growth velocity  $v$  (section 2). Finally, in order to limit computational labour, all of the above approximations are confined to a thin zone of computational cells around the zero level set; this is known as the narrow band level set method introduced by Adalsteinsson and Sethian [45]. The narrow band width must have an upper bound dependent on the curvature of the level sets, or dependent on the size of the speed function. Once the front moves out of this thin zone, Sethian’s fast marching method [46] is used to rebuild a new narrow band centred around the current position of the interface.

This work uses a narrow band level set formulation [45] to characterize and advance the evolving interface. For details about the theory, algorithms, and applications of level set methods, the reader is referred to [7].

#### 4. Simulations

Consider a solid being subject to non-hydrostatic stress ( $\sigma_1$ ) as shown in figure 3. We examine the interface growth of the stressed crystal/amorphous system from  $t = 0$  to 7000 s. The interface is ‘prerippled’ so that it has a sine-wave shape of amplitude  $A = 10$  nm and wavelength  $\lambda = 400$  nm. Since the interface rippling is in one direction, the sample may be treated as a two-dimensional solid. We assume plane stress for the elastic solids analyses. The interface velocity (normal to the interface) is determined by using equation (1) in section 2.

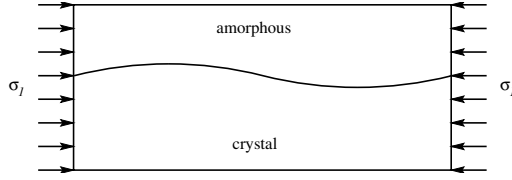


Figure 3. Amorphous/crystal interface in a stressed solid.

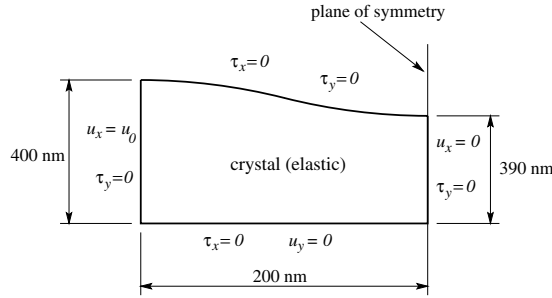


Figure 4. Geometry and BCs for the simulation with stress-free amorphous phase.

The velocity is a function of a number of variables, including surface stress, orientation, and curvature at each point on the interface.

Three cases are studied in this work. In the following calculations, only a half wavelength segment of the interface is considered.

#### 4.1. Stress-free amorphous case

It is assumed here that there is no stress in the amorphous phase, thus this interface is traction free ( $\tau = \mathbf{0}$ ). Since the left-hand surface of the crystal is kept planar during the experiment, instead of  $(\tau_x = \sigma_1, \tau_y = 0)$ ,  $(u_x = u_0, \tau_y = 0)$  is used as the boundary condition (BC), where  $u_0 = S_{11}\sigma_1\lambda/2$  and  $S_{11}$  is an elastic constant derived from the strain–stress relations  $\epsilon_i = S_{ij}\sigma_j$ . The BC at the bottom of the crystal is  $(\tau_x = 0, u_y = 0)$  while that on the right-hand side is  $(u_x = 0, \tau_y = 0)$  due to symmetry (see figure 4).

The interface's velocity normal to itself is determined by using equation (1) (section 2). The stress state of the interface is computed via the post-processing Galerkin method (discussed in section 3.1.3) after the unknown displacements and tractions on the boundary are obtained by the SGBIM. Finally, the interface growth can be determined from its velocity by using level set methods. The flowchart (figure 5) represents the algorithm used for determining the interface growth.

#### 4.2. Elastic amorphous case

Here, both crystalline and amorphous Si are taken into account and amorphous Si is assumed to have elastic behaviour. Elastic constants of amorphous Si can be found in [10], and the following relationship between the elastic constants of the amorphous and crystalline Si is employed in this work:

$$G_a = 0.79G_c \quad \nu_a = \nu_c. \quad (33)$$

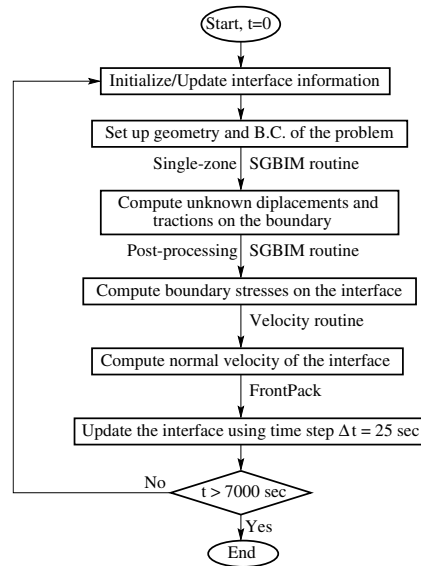


**Figure 5.** Basic flowchart for computing interface growth (stress-free amorphous case).

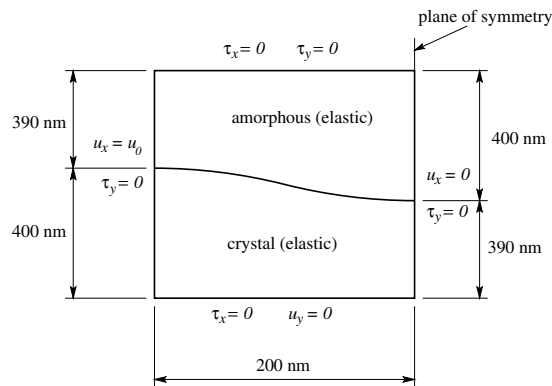


**Figure 6.** Geometry and BCs for the simulation with elastic amorphous phase.

In this situation, the elastic domain contains a bi-material interface where unknown physical quantities need to be found such that they satisfy continuity conditions across the interface. Again, the SGBIM for elasticity can be used to solve this problem [47]. The geometry and BCs of the problem are shown in figure 6. Once the displacements and tractions on the boundary and interface of crystalline Si are obtained, boundary stresses on the crystal interface can be found in the same manner as described in section 3.1.1. Therefore, the only difference between the flowcharts of this case and the stress-free amorphous case is that a SGBIM routine for multi-zone problems is employed instead of that for a single zone.

#### 4.3. Viscous amorphous case

In this case, the amorphous phase is assumed to be an incompressible Newtonian fluid that is governed by the Navier–Stokes equation. For this experiment, the half wavelength along the

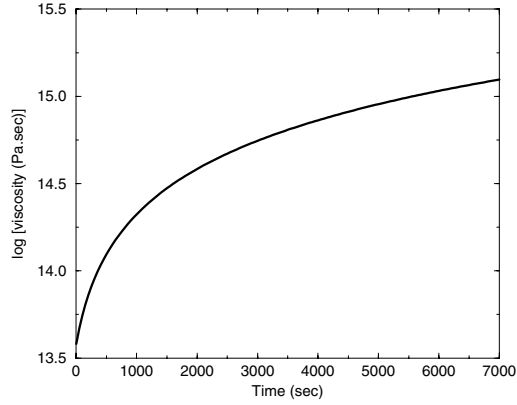


Figure 7. Time-dependent viscosity of the amorphous Si.

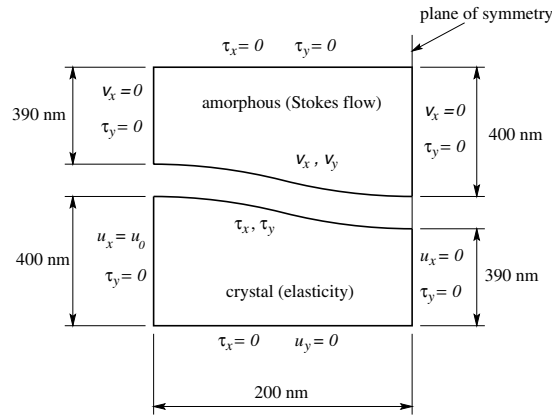


Figure 8. Geometry and BCs for the simulation with viscous amorphous phase.

interface is  $\lambda/2 = 200 \text{ nm} = 2 \times 10^{-7} \text{ m}$ , the velocity imposed on the viscous fluid at the interface (which is defined below in (36)) is approximately  $v \simeq 7 \times 10^{-16} \text{ m s}^{-1}$ , the density of the amorphous Si is  $\rho \simeq 2.3 \times 10^3 \text{ kg m}^{-3}$ , and the minimum viscosity (as  $t = 0 \text{ s}$ , see figure 7) is  $\mu \simeq 10^{13.6} \text{ Pa s}$ . Thus, the Reynolds number

$$Re = \frac{v\lambda\rho}{2\mu} \simeq 8 \times 10^{-33} \ll 1. \quad (34)$$

For  $Re \ll 1$ , the Navier–Stokes equation reduces to the Stokes equation (see [40], for example) and the amorphous Si can be considered as a Stokes flow. As a result, the BCs of the amorphous problem only involve tractions and velocities on the boundary. These BCs are shown in figure 8 where the BCs of the crystal problem are similar to those in the elastic amorphous case. Here, the continuity condition across the interface requires that tractions on the amorphous and crystal interfaces should be counterbalanced.

The flowchart (figure 9) describes the algorithm employed for determining the interface growth in this case. First, it is recalled that the unknowns on the boundary of the crystal or amorphous problems can be found by solving the following linear system constructed by the SGBIM:

$$A\mathbf{u} = \mathbf{b} \quad (35)$$

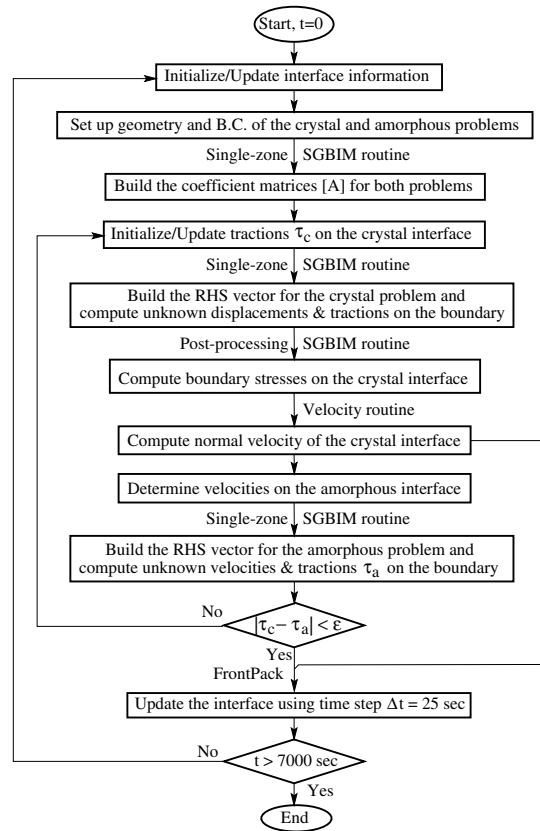


**Figure 9.** Basic flowchart for computing interface growth (viscous amorphous case).

where  $\mathbf{A}$ ,  $\mathbf{u}$  and  $\mathbf{b}$  are the coefficient matrix, vector of unknowns, and right-hand side (RHS) vector, respectively.

During the iteration to determine tractions on the interface at a given time  $t$ , only the boundary values on the crystal and amorphous interfaces change. Thus, the coefficient matrices  $\mathbf{A}$  for both problems are unchanged and they should be constructed using the SGBIM routine before the iterative calculation.

At a given time  $t$ , tractions  $\tau_c$  on the crystal interface need to be initialized. At  $t = 0$ , the iteration begins with  $\tau_c = \mathbf{0}$ . The converged tractions at a given time are then used to initialize tractions at the next time step. Once  $\tau_c$  are initialized/updated, the RHS vector can be built and system (35) is solved. A post-processing SGBIM routine and a velocity routine are then used to compute boundary stresses and velocities  $v_c$ , respectively, on the crystal interface.

A key step in obtaining the continuity condition across the interface is determining the velocity  $v_a$  of the amorphous interface at a given time. This velocity results from the relaxation of stress in the crystal due to the change in shape of the interface as it grows. The rate of displacement change  $\Delta u$  on the crystal interface induces the velocity of the amorphous interface

$$v_a \approx \frac{\Delta u}{\Delta t}. \quad (36)$$

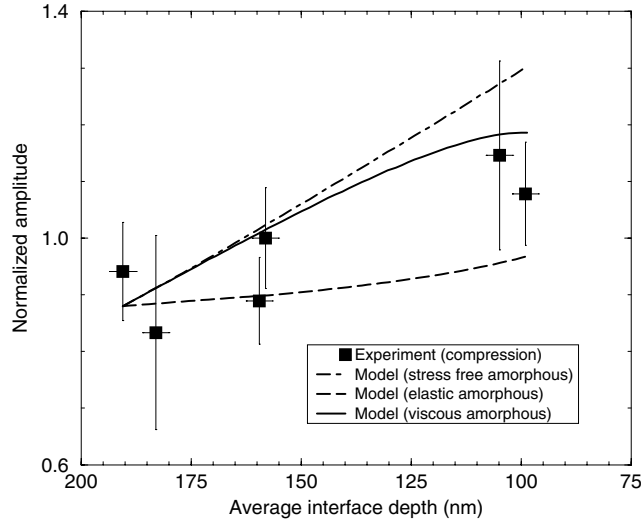


Figure 10. Perturbation amplitude versus distance grown (compression).

Once  $v_a$  is determined, the RHS vector can be built and system (35) can be solved to obtain tractions  $\tau_a$  on the amorphous interface. If tractions on both interfaces are counterbalanced or the criterion  $|\tau_c - \tau_a| < \epsilon$  is satisfied,  $v_c$  is supplied to FrontPack (a level set library of routines used for solving problems involving the evolution of moving interfaces) in order to advance the crystal interface; otherwise,  $\tau_a^{(i)}$  of the current time step is used to update tractions  $\tau_c^{(i+1)}$  of the next time step on the crystal interface as follows:

$$\tau_c^{(i+1)} = \tau_c^{(i)} + k_r \tau_a^{(i)} \quad (37)$$

where  $k_r$  is a relaxation coefficient, and the calculation is iterated towards convergence.

## 5. Results and discussion

In figure 10, the results for growth under compression are plotted for all three models, together with the experimental data [4]. The experimental values of the interface ripple are normalized by the amplitude of the surface corrugation in order to account for sample-to-sample variations in the latter. The abscissa is the average depth of the interface below the free surface. It decreases with time as the amorphous phase transforms to crystalline form. All three models predict a growth instability, i.e. the amplitude of the ripple grows as the crystal grows. The *stress-free amorphous* model overestimates the amplitude growth while the *elastic amorphous* model underestimates the growth. The *viscous amorphous* model gives the best fit to the experiment. While there is a lot of scatter in the experiments it appears that this model still slightly overestimates the amplitude growth. Figure 11 shows a series of seven snapshots of the interface as it evolves under compression for the viscous amorphous model.

In figure 12, the results for crystal growth under tension are plotted for the three models. The models all predict a decrease in amplitude as the crystal grows. The stress-free amorphous model overestimates the rate at which the amplitude dies off while the elastic amorphous model underestimates it. Again the best fit is provided by the viscous amorphous model. While recognizing that there is only one data point for the tension case, it appears the viscous amorphous model slightly overestimates the rate of amplitude reduction.

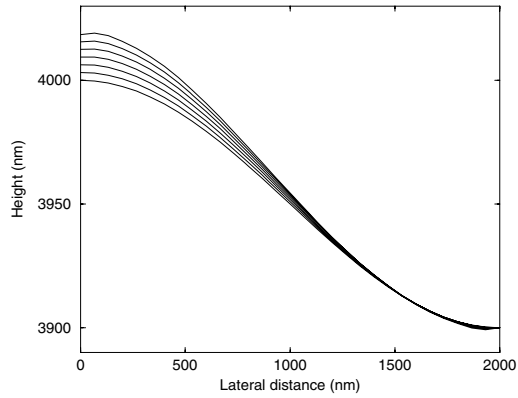


**Figure 11.** Snapshots of the interface evolution for the viscous amorphous case under compression. Each successive curve is plotted after a time step of 500 s.

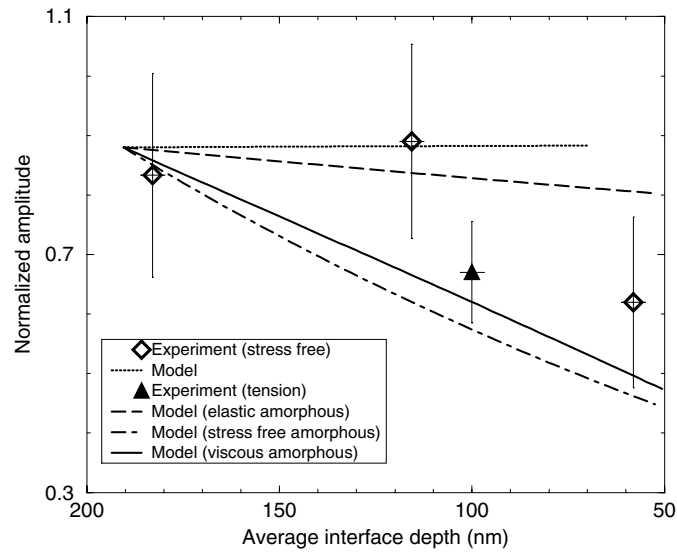


**Figure 12.** Perturbation amplitude versus distance grown (tension and stress free).

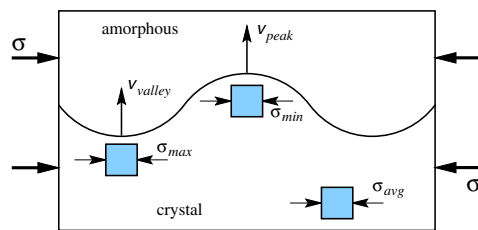


**Figure 13.** Origin of instability.

The calculations show that the instability is driven by the change in the growth rate at the interface due to the variation of stress along the rippled interface (see figure 13). Stress

concentrates in the valleys of the crystal interface and is relieved in the peaks. The effect of the stress on the mobility of the atoms in the interface (the term  $\sigma V^*$  in the velocity equation (1)) dominates the growth process. For compressive stress, the growth rate is slowed. Since the compressive stress is greater in the valleys than in the peaks, the peaks are slowed down less than the valleys and the amplitude grows. For tensile stress, the growth rate is increased. Now the concentration of stress in the valleys speeds them up more than the peaks are speeded up and the amplitude decreases.

The small tendency of the viscous amorphous model to overestimate the rates of amplitude increase and decrease for the compression and tension cases, respectively, may be a result of assuming a viscous fluid model for the amorphous phase. In fact, the extremely small Reynolds number calculated in section 4.3 for this experiment indicates that a viscous-elastic model for the amorphous phase may be needed. Since in both the compression and tension cases, the viscous amorphous result can be improved by moving it slightly towards the elastic amorphous result, a viscous-elastic model for the amorphous phase should improve the accuracy of the simulation.

For completeness, interface evolution is considered in the absence of stress. The result is shown in figure 12. In this case, all three models give the same result. The only terms that contribute in the absence of applied stress are the curvature term,  $\Delta G_\kappa$ , and the angular dependence of the velocity term,  $v_0(\theta)$ . The angular term dominates in this case and the result of the simulation is very sensitive to the form of this angular term. We have used a relatively crude fit to the measured angular dependence of the velocity.

One process that is only partially included in the model is the flow induced in the amorphous silicon to account for the density difference between the crystal and amorphous phases. The crystal is approximately 1.7% denser than the amorphous phase. As a result, there is a flow of silicon atoms in the amorphous phase towards the interface that plays a part in determining the rate of crystallization. The flow is sustained in the amorphous material by a density gradient. The fitting of the velocity function to experiment automatically includes this effect for a flat interface where the flow is uniform. However, when the interface is rippled the flow develops a non-uniform component and this may slightly alter the crystallization rate. The contribution from the non-uniform part of the flow should be very small for the problem we are considering.

For modelling the silicon phase transformation experiment, a two-dimensional calculation was appropriate. Simulating a more general geometry where three-dimensional (3D) calculations would be necessary appears to be quite feasible. The analogous 3D boundary integral and level set techniques are well established and available. The only missing piece of a 3D algorithm is a remeshing routine that automatically converts the level set surface points into a suitable mesh of the interface for the BIM calculation (in two dimensions, this is trivial). Regarding the physics, the only significant changes in the interface phase transformation equation would be in the description of the angular dependence of the growth velocity, and in the treatment of the interface curvature.

## 6. Conclusions

We have developed an accurate method based on advanced numerical techniques for modelling crystal growth in a stressed solid. The numerical methods include advanced boundary integral analysis to model the elastic solids and viscous fluid, and level set methods to treat the moving boundaries. The coupling of boundary integral and level set methods for moving boundary problems appears to be highly effective [48]. We used this method to model the growth of crystal silicon from the amorphous phase. Our results compare very favourably with experiment and strongly support the proposed kinetic mechanism for the observed interface

growth instability. These methods will be applied to a number of new applications involving phase transformations and chemical reactions in solids.

### Acknowledgments

This research was supported in part by the Applied Mathematical Sciences Research Program of the Office of Mathematical, Information, and Computational Sciences, US Department of Energy under contract DE-AC05-00OR22725 with UT-Battelle, LLC, and under contract DE-AC03-76SF00098 with the University of California. Additional support was provided by the ORNL Laboratory Directed Research and Development Program of the Oak Ridge National Laboratory. Work at Harvard was supported by NSF-DMR-98-13803. Work at Berkeley was also supported by the Division of Mathematical Sciences of the National Science Foundation, and the Office of Naval Research under grant FDN00014-96-1-0381. DA acknowledges the support from the Alfred P Sloan Foundation, and WB-C acknowledges the support from NSF and DARPA through cooperative agreement DMS-9615854 as part of the Virtual Integrated Prototyping Initiative.

### References

- [1] Asaro R J and Tiller W A 1972 *Metall. Trans.* **3** 789
- [2] Grinfeld M A 1986 *Sov. Phys.-Dokl.* **31** 831
- [3] Srolovitz D J 1989 *Acta Metall.* **37** 621
- [4] Barvosa-Carter W, Aziz M J, Gray L J and Kaplan T 1998 *Phys. Rev. Lett.* **52** 1445
- [5] Sage J F, Barvosa-Carter W and Aziz M J 2000 *Appl. Phys. Lett.* **77** 516
- [6] Voorhees P W and Aziz M J 1999 *Proc. Conf. on Interfaces for the Twenty-First Century* (London: Imperial College Press)
- [7] Sethian J A 1999 *Level Set Methods and Fast Marching Methods* (New York: Cambridge University Press)
- [8] Gray L J, Chisholm M F and Kaplan T 1993 *Boundary Element Technology VIII (BETECH-93)* ed H Pina and C A Brebbia (Computational Mechanics Publications) p 181
- [9] Barvosa-Carter W 1997 *PhD Thesis* Harvard University
- [10] Witvrouw A and Spaepen F 1993 *J. Appl. Phys.* **74** 7154
- [11] Csepregi L, Kennedy E F, Mayer J W and Sigmon T W 1978 *J. Appl. Phys.* **49** 3906
- [12] Khoptiar Y and Aziz M J, unpublished
- [13] Olson G L and Roth J A 1993 *Solid phase epitaxy Handbook of Crystal Growth 3: Thin Films and Epitaxy* ed D T J Hurlle (Amsterdam: Elsevier) ch 7
- [14] Barvosa-Carter W and Aziz M J 1995 *Mater. Res. Soc. Symp. Proc.* **356** 87
- [15] Barvosa-Carter W and Aziz M J 1997 *Mater. Res. Soc. Symp. Proc.* **441** 75
- [16] Barvosa-Carter W and Aziz M J 2001 *Appl. Phys. Lett.* at press
- [17] Donovan E P, Spaepen F, Turnbull D, Poate J M and Jacobson D C 1985 *J. Appl. Phys.* **57** 1795
- [18] Yang C M 1997 *PhD Thesis* California Institute of Technology
- [19] Bernstein N, Aziz M J and Kaxiras 1998 *Phys. Rev. B* **58** 4579
- [20] Custer J S *et al* 1990 *Mater. Res. Soc. Symp. Proc.* **157** 689
- [21] Cowley E R 1988 *Phys. Rev. Lett.* **60** 2379
- [22] Feynman R P, Leighton R B and Sands M 1966 *The Feynman Lectures on Physics* vol II (Reading, MA: Addison-Wesley) p 396
- [23] Kittel C 1967 *Introduction to Solid State Physics* 3rd edn (New York: Wiley) p 112
- [24] Bonnet M 1995 *Boundary Integral Equation Methods for Solids and Fluids* (Chichester: Wiley)
- [25] Bonnet M, Maier G and Polizzotto C 1998 *ASME Appl. Mech. Rev.* **51** 669
- [26] Rizzo F J 1967 *Q. Appl. Math.* **25** 83
- [27] Gray L J 1991 *Math. Comput. Model.* **15** 165
- [28] Martin P A and Rizzo F J 1989 *Int. J. Num. Methods Eng.* **421** 341
- [29] Krishnasamy G, Rizzo F J and Rudolphi T J 1992 *Comput. Mech.* **9** 267
- [30] Martin P A and Rizzo F J 1996 *Int. J. Num. Methods Eng.* **39** 687
- [31] Richardson J D, Cruse T A and Huang Q 1997 *Comput. Mech.* **20** 213

- [32] Cruse T A and Richardson J D 1996 *Int. J. Num. Methods Eng.* **39** 3273
- [33] Martin P A, Rizzo F J and Cruse T A 1998 *Int. J. Num. Methods Eng.* **42** 885
- [34] Gray L J and Griffith B 1998 *Commun. Num. Methods Eng.* **14** 1109
- [35] Balakrishna C, Gray L J and Kane J H 1994 *Comput. Meth. Appl. Mech. Eng.* **111** 335
- [36] Frangi A and Novati G 1996 *Comput. Mech.* **19** 58
- [37] Hölzer S M 1993 *Commun. Num. Meth. Eng.* **9** 219
- [38] de Paula F A and Telles J C F 1989 *Eng. Anal. Bound. Elements* **6** 123
- [39] Gray L J 1998 *Advances in Boundary Elements Series: Singular Integrals in Boundary Element Methods* ed V Sladek and J Sladek (Boston, MA: Computational Mechanics) ch 2
- [40] Pozrikidis C 1992 *Boundary Integral and Singularity Methods for Linearized Viscous Flow* (New York: Cambridge University Press)
- [41] Gray L J, Maroudas D and Enmark M N 1998 *Comput. Mech.* **22** 187
- [42] Osher S and Sethian J A 1988 *J. Comput. Phys.* **79** 12
- [43] Sethian J A 1985 *Commun. Math. Phys.* **101** 487
- [44] Sethian J A 1987 *Numerical Methods for Propagating Fronts in Variational Methods for Free Surface Interfaces* ed P Concus and R Finn (New York: Springer)
- [45] Adalsteinsson D and Sethian J A 1995 *J. Comput. Phys.* **118** 269
- [46] Sethian J A 1996 *Proc. Natl Acad. Sci.* **93** 1591
- [47] Maier G, Diligenti M and Carini A 1991 *Comput. Meth. Appl. Eng.* **92** 193
- [48] Sethian J A and Strain J D 1992 *J. Comput. Phys.* **98** 231